A&A 471, 929–939 (2007)
DOI: 10.1051/0004-6361:20077601

Astronomy & Astrophysics

X-ray flares on the UV Ceti-type star CC Eridani: a "peculiar" time-evolution of spectral parameters⋆

I. Crespo-Chacón[1,2], G. Micela[1], F. Reale[1,3], M. Caramazza[1,3], J. López-Santiago[1,⋆⋆], and I. Pillitteri[3]

[1] INAF – Osservatorio Astronomico di Palermo, Piazza del Parlamento 1, 90134 Palermo, Italy
e-mail: [ichacon;giusi;jlopez]@astropa.unipa.it
[2] Departamento de Astrofísica, Facultad de Ciencias Físicas, Universidad Complutense de Madrid, 28040 Madrid, Spain
e-mail: icc@astrax.fis.ucm.es
[3] Dip. di Scienze Fisiche e Astronomiche – Sez. di Astronomia – Università di Palermo, Piazza del Parlamento 1, 90134 Palermo, Italy
e-mail: [reale;mcarama;pilli]@astropa.unipa.it

Received 3 April 2007 / Accepted 7 June 2007

ABSTRACT

Context. Weak flares are supposed to be an important heating agent of the outer layers of stellar atmospheres. However, due to instrumental limitations, only large X-ray flares have been studied in detail until now.
Aims. We used an XMM-Newton observation of the very active BY-Dra type binary star CC Eri in order to investigate the properties of two flares that are weaker than those typically studied in the literature.
Methods. We performed time-resolved spectroscopy of the data taken with the EPIC-PN CCD camera. A multi-temperature model was used to fit the spectra. We inferred the size of the flaring loops using the density-temperature diagram. The loop scaling laws were applied for deriving physical parameters of the flaring plasma. We also estimated the number of loops involved in the observed flares.
Results. A large X-ray variability was found. Spectral analysis showed that all the regions in the light curve, including the flare segments, are well-described by a 3-T model with variable emission measures but, surprisingly, with constant temperatures (values of 3, 10 and 22 MK). The analysed flares lasted ∼3.4 and 7.1 ks, with flux increases of factors 1.5−1.9. They occurred in arcades made of a few tens of similar coronal loops. The size of the flaring loops is much smaller than the distance between the stellar surfaces in the binary system, and even smaller than the radius of each of the stars. The obtained results are consistent with the following ideas: (i) the whole X-ray light curve of CC Eri could be the result of a superposition of multiple low-energy flares; and (ii) stellar flares can be scaled-up versions of solar flares.

Key words. X-rays: stars – stars: coronae – stars: activity – stars: flare – stars: late-type – stars: individual: CC Eri

1. Introduction

Solar-like stars (main sequence stars with spectral types from F to early M) have radiative cores and convective outer envelopes. Convection, together with differential rotation, generates a magnetic dynamo (see Parker 1975, and references therein) that is responsible of the formation of the corona (see Favata & Micela 2003 and Güdel 2004, for two extensive reviews about stellar coronal astronomy). Magnetic activity similar to that observed on the Sun is typically detected on these stars, showing variability through all the electromagnetic spectrum. The activity level of a star is frequently measured in terms of its coronal X-ray luminosity L_X. Using data collected by the ROSAT satellite, Schmitt et al. (1995) and Schmitt (1997) found that solar-like stars present X-ray luminosities (integrated over the 0.1−2.4 keV energy band) in the range $25.5 \lesssim \log L_X(\mathrm{erg\,s^{-1}}) \lesssim 29.5$. This luminosity is correlated with the stellar rotation rate (Pallavicini et al. 1981). Walter (1982) noticed that a single power law dependence between L_X/L_{bol} and the angular velocity was unable to reproduce all the observed data, and proposed to replace it by either a broken power law or an exponential relationship. This result later led to the concept of saturation of stellar activity at high rotation rates (Vilhu 1984; Vilhu & Walter 1987). Rotational velocity, and therefore activity, decreases with age because of the angular momentum losses due to the magnetised stellar wind (Rengarajan 1984; Pace & Pasquini 2004). However, short-period binaries can maintain high rotation rates since they are synchronized by tidal coupling.

Flares are the most extreme evidence of magnetic activity in stellar atmospheres. Frequent flaring is found on late K and M dwarfs in the solar neighbourhood (the so-called UV Ceti-type stars – see their general properties in Pettersen 1991). Similarities between solar flares and those observed on UV Ceti-type stars suggest that they are produced by the same basic physical mechanisms. Flares are supposed to be the result of the energy release from magnetic field reconnection in the lower corona (e.g. Kopp & Pneuman 1976). In consequence, electrons and ions are accelerated and gyrate downward along the magnetic field lines, producing synchrotron radio emission. Bremsstrahlung radiation is emitted in hard X-rays (>20 keV) when these ionized beams collide with the denser material of the chromosphere. At the same time, the gas in the affected chromospheric region is heated (optical and UV radiation is then emitted) and evaporated. Thus, the density and temperature of the

⋆ Based on observations obtained with XMM-Newton, an ESA science mission with instruments and contributions directly funded by ESA Member States and NASA.

⋆⋆ Presently at Departamento de Astrofísica, Facultad de Ciencias Físicas, Universidad Complutense de Madrid, 28040 Madrid, Spain (jls@astrax.fis.ucm.es).

newly formed coronal loops increase, emitting in soft X-ray and extreme UV wavelengths. Recent evidence in favour of this scenario was given by Mitra-Kraev et al. (2005) and Smith et al. (2005).

A recurrent idea in the literature is that flares are the main heating agent of the outer stellar atmospheres (e.g. Audard et al. 2000), so that the observed "quiescent" emission would be the result of a superposition of multiple small flares (named "nano-flares"). The distribution law that gives the number of flares dN within an energy-interval $[E, E + \mathrm{d}E]$ allows us to estimate the energy budget of the corona. In particular, solar flares are distributed following a power law (Datlowe et al. 1974; Lin et al. 1984; Dennis 1985), that is

$$\frac{\mathrm{d}N}{\mathrm{d}E} = k_1 E^{-\alpha}, \tag{1}$$

where k_1 is a constant and α is the power-law index. For $\alpha > 2$, an extrapolation of Eq. (1) to flare energies below the detection threshold would be sufficient to account for the luminosity of the quiescent corona. For this reason, it is crucial to investigate the validity of such an extrapolation (Hudson 1991), as well as the value of α on magnetically active stars. For the Sun, values of α between 1.5 and 2.6 were reported (Crosby et al. 1993; Porter et al. 1995; Krucker & Benz 1998). However, a later study carried out by Aschwanden et al. (2000) suggests the insufficiency of nano-flares to heat the solar corona. On the other hand, for active stars, Collura et al. (1988) and Osten & Brown (1999) found $\alpha \approx 1.5-1.6$, while other authors have reported $\alpha > 2$ (Audard et al. 1999, 2000; Kashyap et al. 2002; Güdel et al. 2003). Therefore, it is still unclear if Eq. (1) can be extrapolated from large observable flares towards the weakest ones in order to support the flare-heating hypothesis.

While flare stars have been studied in the optical during more than half a century, the first sizeable sample of X-ray flares was only compiled after the launch of the *Einstein* Observatory (Haisch 1983). Later, Pallavicini et al. (1990) presented the results of a comprehensive survey of X-ray observations of flare stars carried out with the EXOSAT Observatory. However, until recent years, and due to instrumental limitations, only large X-ray flares could be studied in detail. At the present time, the great sensitivity, wide energy range, high energy resolution, and continuous time coverage of the EPIC (European Photon Imaging Cameras) detectors – on-board the XMM-Newton satellite – also enable the detection and analysis of smaller flares. UV Ceti-type flare stars are specially indicated for this purpose because of its proximity. For all these reasons, we decided to carry out the present study of the X-ray flares detected on the UV Ceti-type star CC Eri using the XMM-Newton satellite.

CC Eri (HD 16157) is a spectroscopic binary star (BY Dra-type) located in the immediate solar neighbourhood, at a distance of 11.51 ± 0.11 pc (from Hipparcos, Perryman et al. 1997). This is a SB2 system (Strassmeier et al. 1993) which consists of a K7.5Ve primary and a M3.5Ve secondary (Amado et al. 2000), with mass ratio $\approx$2 (Evans 1959; Amado et al. 2000). The photometric period – 1.56 days – results to be equal to that of the orbital motion (Evans 1959; Bopp & Evans 1973; Bopp & Fekel 1977). Thus, the synchronization due to the tidal lock makes the primary component to be one of the fastest rotating late K dwarfs in the solar vicinity. Using kinematical criteria, the age of the system was estimated to be 9.16 Gyr (Demircan et al. 2006). Busko et al. (1977) and Amado et al. (2000) found that the chromospheric emission of CC Eri varies in antiphase with its optical continuum, suggesting the presence of active emission regions associated with starspots. Besides, its quiescent radio emission is polarized at the 10−20% level (Osten et al. 2002; Slee et al. 2004), indicating large-scale ordering in the stellar magnetic field. CC Eri presents a strong flare activity over a wide range of energies (Busko & Torres 1976, 1978; Caillault et al. 1988; Byrne et al. 1992; Güdel 1992; Pan & Jordan 1995; Amado et al. 2000; Osten et al. 2002; Slee et al. 2004). First X-ray detections of CC Eri were done with HEAO1, showing $\log L_{\mathrm{X}}(\mathrm{erg\,s^{-1}}) \approx 29.26$ in the 2−20 keV band (Tsikoudi 1982), *Einstein*, which measured $\log L_{\mathrm{X}}(\mathrm{erg\,s^{-1}}) \approx 29.51$ in the 0.15−4.5 keV range (Caillault 1982), and EXOSAT, that observed $\log L_{\mathrm{X}}(\mathrm{erg\,s^{-1}}) \approx 29.62$ in the 0.04−2 keV interval (Pallavicini et al. 1988). However, since none of these observations lasted very long, little information on the temporal and spectral variation of the source in X-rays was available. Pan & Jordan (1995) observed and analysed for the first time an X-ray flare on CC Eri, using ROSAT observations. They measured a quiescent luminosity $\log L_{\mathrm{X}}(\mathrm{erg\,s^{-1}}) \approx 29.40$ in the 0.17−2 keV band. The flare had an e-folding rise and decay times of about 1 h (or less) and 2 h, respectively, and the emission was enhanced by a factor greater than 2. A 2-T model gave an adequate description to all the ROSAT spectra and showed the presence of high-temperature plasma (∼10 MK) even during the time-intervals where no flare activity was detected. This is consistent with the results obtained for the quiescent emission of M-dwarfs using data from the EXOSAT ME and *Einstein* IPC (e.g. Pallavicini et al. 1990; Schmitt et al. 1990). All the X-ray luminosities measured for CC Eri are similar and place this binary star among the most active ones. This is clearly noticed when comparing the quiescent X-ray luminosity obtained for CC Eri from the data analysed in this work ($L_{\mathrm{X,\,0.1-2.4\,keV}} \approx 3.7 \times 10^{29}$ erg s^{-1}) with the cumulative X-ray luminosity distribution functions found by Schmitt et al. (1995) for low-mass stars in the solar neighbourhood.

In this paper, we present the study of an XMM-Newton observation of CC Eri, which, for the first time, reveals details about the behaviour of the parameters that characterized the plasma during two flares weaker than those typically analysed in other active dM stars. Technical information about the observation and details of the data analysis is given in Sect. 2. In Sect. 3 we describe the light curve and the different kinds of variations observed. The time-resolved study of spectral parameters is presented in Sect. 4, where we also estimate the size of the flaring loops. Finally, in Sect. 5, we discuss and interpret the results in the context of solar and stellar flares.

2. Observations and data analysis

The observation of CC Eri analysed in this work was performed with the XMM-Newton satellite on August 8, 2003 (PI: H. Kay, ID: 0148790101) during revolution 0671. The XMM-Newton satellite owns the most sensitive soft X-ray detector system presently available: the EPIC instrument. It consists of three imaging and non-dispersive CCD-based cameras: the twin MOS 1 and MOS 2, and the PN (Turner et al. 2001; Strüder et al. 2001). The wavelength range measured by the EPIC detectors allows one to obtain a reliable determination of properties of the hottest plasma components. For our timing and spectral analysis, we used only the data from the PN-CCD camera, that is more sensitive than the MOS detectors. This observation was done in the full frame mode with the thick filter. The exposure time of the image taken with EPIC-PN was 36.703 ks, that is, 0.27 times the orbital period of the binary star CC Eri.

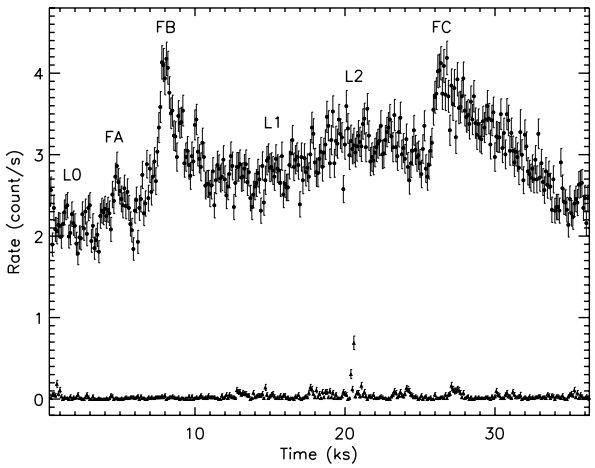

Fig. 1. Source (upper region) and background (lower region) light curves of CC Eri as observed with the EPIC-PN detector for the energy band 0.5−10.0 keV and a temporal binning of 100 s. The labels FA, FB and FC refer to the detected flares while L0, L1 and L2 designate different emission levels where no clear flare activity was observed.

We used the event file in the PPS data products, which was produced with the standard XMM-Newton Science Analysis System (SAS) software, version 5.4.2. The light curve and the spectra were obtained with standard tools of SAS. The PN responses were generated with the SAS RMFGEN and ARFGEN tasks. The spectral analysis was done with the X-ray spectral fitting package XSPEC V11.3.2 (Arnaud 1996, 2004).

Standard selection criteria were applied for filtering the data (see Ehle et al. 2004). We extracted events in the energy band between 0.5−10.0 keV that triggered only one or two detector pixels at the same time (PATTERN ≤ 4). Data below 0.5 keV were excluded to avoid residual calibration problems in the response matrices at soft energies. Nevertheless, since flares mainly affect hotter thermal components, the spectral region below 0.5 keV is not crucial for our analysis. In fact, we checked that no significant variations are found in the spectral parameters (see Sect. 4.1) when the region 0.3−0.5 keV is included for fitting the spectra. The EPATPLOT task was used for confirming the existence of pile-up affecting the inner region of CC Eri. To lose the minimum number of counts as possible, we looked for and ignored the smallest region that allowed avoiding the pile-up effects during the whole observation. The X-ray light curve and spectra were therefore obtained with the events taken from an annulus with inner radius 12″ and outer radius 44″. On the other hand, background photons were extracted from a source-free region – a circle with a radius of 54.4″ – placed at the same CCD as CC Eri.

3. The light curve

Figure 1 shows the source (background – subtracted) and background light curves of CC Eri as observed with the EPIC-PN detector for a temporal binning of 100 s and the filtering criteria given in Sect. 2. Note that the background count-rate was scaled to the size of the source region. The dead-time correction was applied to both the source and background count-rates. A significant X-ray variability was found throughout the observation. The lowest activity level (L0 or *quiescent state* hereafter) was observed at the beginning. It was followed by a small flare (FA) where the stellar flux increased by a factor 1.3. Another two flares (FB and FC) with flux changes of factors 1.5−1.9, depending on the selected reference level, were also observed. The maxima of these two flares were separated by 5 h. In addition, the stellar emission between these two events was also variable – two different activity levels (L1 and L2) were identified – and higher than that observed during the quiescent state. The start and end times of the main selected periods are summarized in Table 1. FA, FB and FC radiated in the 0.5−10.0 keV band a total energy of 0.08, 0.75 and 1.5×10^{33} erg, respectively.

Table 1. Time-intervals of the main activity levels detected on CC Eri (see Fig. 1).

Activity level	Time-interval (ks after the observation starts)
L0	0.0−3.6
FA	3.6−5.6
FB	5.6−12.9
L1	12.9−17.7
L2	17.7−23.7
FC	23.7−36.7

Table 2. Duration of the rising (τ_R) and decay (τ_D) phases of the flares observed on CC Eri.

Flare	τ_R (s)	τ_D (s)
FA	400	580
FB	570	2850
FC	1100	5960

In terms of relative increasing of flux with respect to the quiescent level, the strength of the detected flares is somewhat smaller than the typical values analyzed on active low-mass stars. For instance, Robrade & Schmitt (2005) found flux increases of factors 2−3 in flares produced by EQ Peg, AT Mic, AD Leo and EV Lac. All of them can be considered as moderate flares in view of the flux increases (10−300 times the quiescent state value) that Favata et al. (2000c), Katsova et al. (2002), and Güdel et al. (2004) observed respectively on EV Lac, EQ Peg and Prox Cen. The detected flares are even a little bit weaker than that observed by Pan & Jordan (1995) on the same star, CC Eri, which showed a ratio between the peak and minimum fluxes larger than a factor of 2. However, in absolute terms, the peak X-ray luminosity of the analysed flares is large compared to that of the brightest solar flares.

Table 2 lists the duration of the rising and decay phases of the observed flares. Since the behaviour of these two phases can be well-described by an exponential law, their duration was respectively estimated as the $1/e$ rise time (τ_R) or $1/e$ decay time (τ_D). The values of τ_R and τ_D were therefore determined from a least-squares fit to the corresponding data by an exponential function of the form $R = A_0 e^{(t-t_{max})/\tau} + R_{base}$; where R is the count-rate, R_{base} is the count-rate in the quiescent state (L0 in this case), A_0 is the amplitude at the flare maximum, t is the time, t_{max} is the time at the flare maximum, and τ is τ_R or $-\tau_D$. Note in Fig. 1 that flare FC could have a larger or shorter decay time, depending on the value considered for R_{base} (i.e., equal to that of L0 or, on the contrary, L1), but being always greater than 50 min. Using data collected by the LE experiment on EXOSAT, Pallavicini et al. (1990) found two different types of flares in a sample of 32 M dwarf stars, i.e., *impulsive flares* and *long decay flares*, similar to the ones observed on the Sun (Pallavicini et al. 1977). Those in the first group are reminiscent of solar *compact* flares, showing rise times of a few minutes and decay times of tens of minutes; and those in the second group, with decay times of the order of ≈1 h or longer, are reminiscent of solar long-duration *2-ribbon*

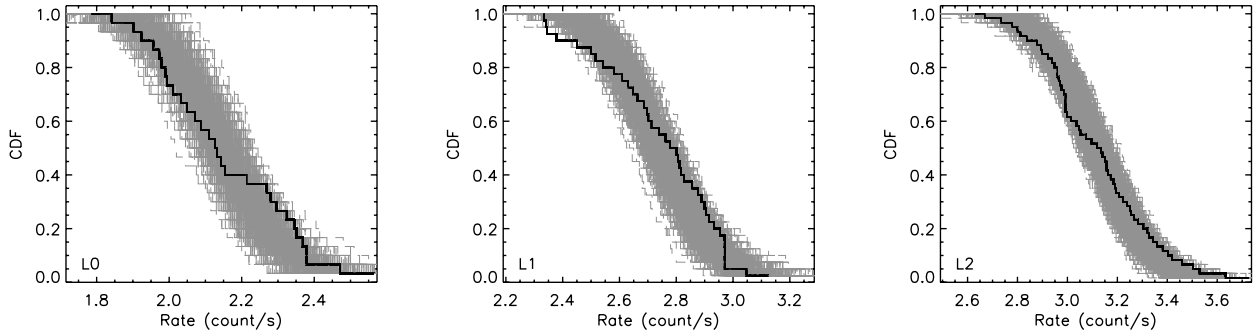

Fig. 2. Cumulative distribution function of the count-rates observed in the regions L0, L1 and L2 (solid black line) compared to those simulated by supposing a constant source with count-rate equal to the mean value (R_m[Li]) in the given region (dashed area).

flares. Thus, FA can be classified as an impulsive flare and FC as a long decay one. However, the classification of flare FB is unclear since its decay time is in the limit range between the two types. As discussed by Pallavicini (1988) and Poletto et al. (1988), these morphological differences may indicate real physical differences in the energy release process, as it also appears to happen for solar compact and 2-ribbon flares (Pallavicini et al. 1977; Priest 1981). In particular, in compact flares energy is probably released only during the impulsive phase, whereas in 2-ribbon flares a prolonged energy release is apparently required to explain their long decay times. Regarding this point, it is interesting to note the peaks observed in the light curve during the decay of flare FB, which are probably related to different magnetic reconnection processes (superposed flare-type events).

3.1. Searching for short-term variability

There are three long intervals in the light curve of CC Eri (L0, L1 and L2) that have been supposed to have a constant emission level. In this section we make use of the method given by Marino et al. (2000) to test whether small changes within each one of these time regions (see Fig. 1) can be considered further short-term stellar variability or, on the contrary, are compatible with statistical fluctuations.

Assuming that during the intervals L0, L1 and L2 the star has a constant count-rate equal to the mean count-rate characteristic of each one of these regions (R_m[Li]), we computed the net counts expected ($c_{exp,\ bin}$[Li]) in the used temporal bin (100 s). For every interval, we generated a set of simulated data with the N Poisson distribution centered on $c_{exp,\ bin}$[Li], which represents possible outcomes from the observations if the source had a constant count-rate equal to the mean count-rate of the interval. Each set consisted of 1000 of such simulations. We then calculated the cumulative distribution function (CDF[1]) of the count-rates observed within the interval, as well as of each one of these simulations. The set of the CDF's obtained for the simulations allowed us to evaluate the spread introduced by statistical fluctuations.

In Fig. 2 we have plotted the CDF of the intervals L0, L1 and L2. All of them are compared with their corresponding simulations for a constant source with count-rate equal to R_m[Li] (dashed area). In all the three cases the CDF of the observed count-rates is contained within the space occupied by the CDF's of the simulations. Therefore, statistical fluctuations can account for the observed spread and possible short-term variability on CC Eri cannot be distinguished from noise in these regions. However, when the analysis is done for the three intervals (L0, L1 and L2) altogether, significant differences between the observations and simulations are found (see Fig. 3). In fact, the same happens when the analysis is separately done for L0 and L1, or L1 and L2. The difference between the emission from L0, L1 and L2 is therefore due to stellar variability and cannot be explained only by statistical fluctuations.

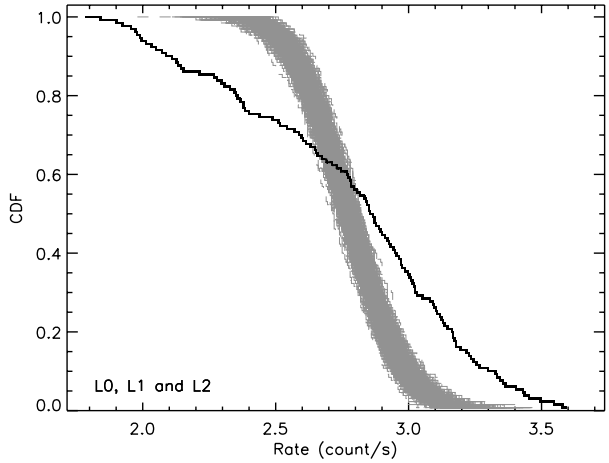

Fig. 3. Cumulative distribution function of the observed count-rates obtained for L0, L1 and L2 altogether (solid black line) compared to those simulated by supposing a constant source with count-rate equal to the mean value of these three regions (dashed area).

The same type of study can also be used to quantify the variations found in the complete light curve of CC Eri (Fig. 4). Since in this case we were looking for changes relative to the quiescent emission, we chose as reference level the mean count-rate measured for the quiescent state, i.e. R_m[L0]. If the duration of the observation were long enough, the CDF could be considered as the fraction of time that the star spends with a count-rate greater than, or equal to, a given value. The tail of the CDF at rate $\gtrsim$3 count/s is produced by the two strongest detected flares (FB and FC). The rest of the CDF not consistent with the simulations accounts for the other kind of variability observed at different time scales on the light curve of CC Eri.

In addition, we analyzed FA to confirm that the emission within this time-interval was not constant. We obtained that the part of the CDF at the highest count-rates of FA is out of the simulations. Therefore, FA is probably a flare-event. However, the current instrumentation did not allow us to carry out a

[1] The cumulative distribution function (CDF) represents the probability of observing a number of counts – in the chosen temporal bin – greater than, or equal to, a given value.

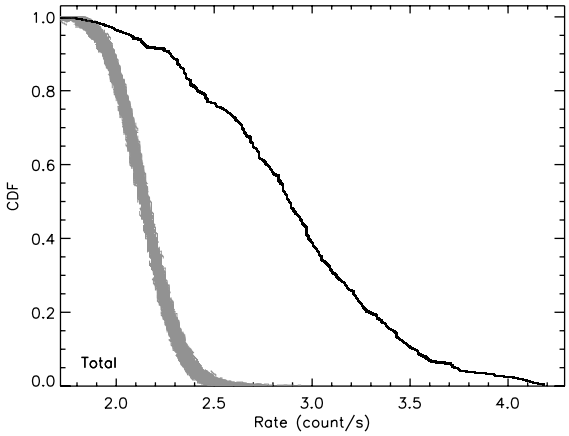

Fig. 4. Cumulative distribution function of the count-rates detected in the whole observation of CC Eri (solid black line) compared to those simulated by supposing a constant source with count-rate equal to the quiescent value (dashed area).

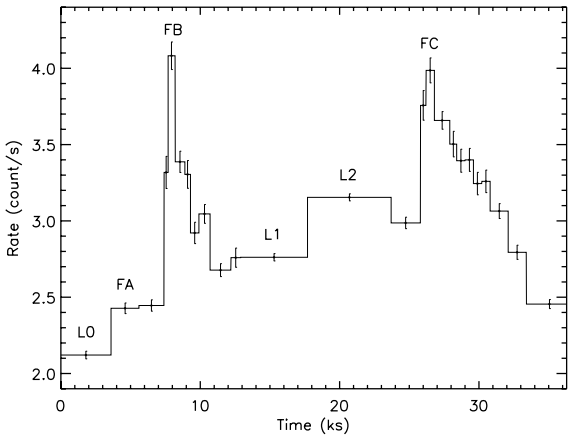

Fig. 5. Rebinned light curve of CC Eri for the energy band 0.5−10.0 keV.

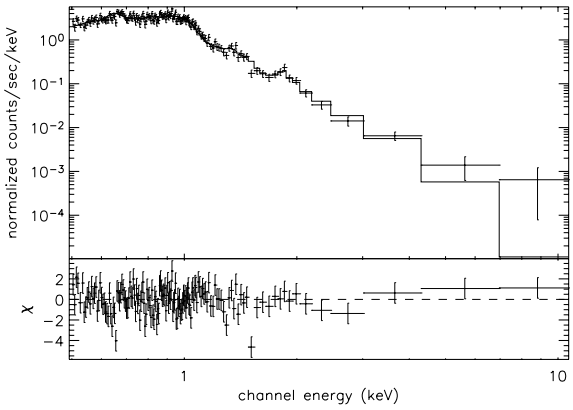

Fig. 6. X-ray spectrum of the quiescent state of CC Eri (L0). The best fit (2-T APEC model) is also shown with a solid line.

time-resolved study of the different phases of FA due to the low strength and shortness of this flare.

4. Spectral analysis

In this section we carry out a time-resolved study of coronal properties (temperature, emission measure and metal abundance) through the whole observation of CC Eri.

With this scope, and taking the variability pattern in the light curve into account, the total observing time was split in several time-intervals with approximately constant count-rate. All the intervals were chosen in order to have enough signal to perform a reliable spectral analysis. Most of the spectra have at least 2000 counts. However, the spectrum extracted for the rising phase of both FB and FC was taken with less photons ($\gtrsim$1000 counts) for avoiding to mix this region with the flare maximum. The rebinned light curve of CC Eri is shown in Fig. 5. We obtained the spectra of all these intervals following the filtering criteria given in Sect. 2. Every spectrum was binned to provide at least 8 counts per spectral bin. Bad channels were always excluded.

We modeled the spectra by using the Astrophysical Plasma Emission Code (APEC, Smith et al. 2001a) included in the XSPEC software. APEC calculates spectral models for hot, optically thin plasmas using atomic data stored in the Astrophysical Plasma Emission Database (APED, Smith et al. 2001b). The APED files contain atomic data such as collisional and radiative rates, recombination cross sections, dielectronic recombination rates, and satellite line wavelengths, which constitute the relevant information for calculating both the continuum and line emission. Interstellar absorption was taken into account by using the photoelectric cross sections of Morrison & McCammon (1983), also available in XSPEC. Despite the generally satisfactory results of using the χ^2 minimization technique for obtaining the best fitted model, it runs into problems when the number of events is small. For this reason, our fit procedure was based on the Cash's C statistic minimization (Nousek & Shue 1989), which gives better fits in the low-count regime (note also that the C statistic is equivalent to χ^2 in the limit of large number of counts). Unfortunately, for the C statistic there exists no method analogous to that of the reduced χ^2 value ($\chi^2_{\rm red}$) with which we can measure the goodness of the fit. We can determine the best parameters by minimizing the function, but we have no criteria for rejecting the model. Therefore, for giving an idea of the goodness of our fits we show the reduced χ^2 value generated by each model (obtained through C statistic minimization) and its corresponding data set. The errors associated with the fitted parameters were calculated for a confidence level of 2.706σ.

A 2-T model was needed to describe the shape of the coronal spectrum of the quiescent state (L0, see Fig. 6). Leaving all the parameters as free variables, and taking the same global abundance (scaled on the solar photospheric values of Anders & Grevesse 1989) for all the temperature components, we obtained the following results: the hydrogen column density ($N_{\rm H}$) of the intervening interstellar medium is negligible in the studied wavelength range, as expected due to the proximity of CC Eri; the global coronal abundance is $Z/Z_\odot = 0.33^{+0.10}_{-0.07}$; the temperatures are $KT_1 = 0.301^{+0.011}_{-0.011}$ keV and $KT_2 = 0.927^{+0.034}_{-0.036}$ keV; and the emission measures for these thermal components are $EM_1 = 1.69^{+0.35}_{-0.31} \times 10^{52}$ cm^{-3} and $EM_2 = 1.50^{+0.30}_{-0.26} \times 10^{52}$ cm^{-3}, that is, $EM_2/EM_1 \approx 0.9$. These values give the best possible fit to the data using the C statistic, corresponding to a $\chi^2_{\rm red} \approx 1.44$.

4.1. Time-resolved study of spectral parameters

We carried out the spectral analysis of all the time-intervals showed in Fig. 5 to examine the influence of the observed flares on the temperatures and emission measures of the plasma. Reale et al. (2001) converted X-ray data of a sample of solar flares into the same format and framework as stellar X-ray data, in the perspective to use them as templates for interpreting

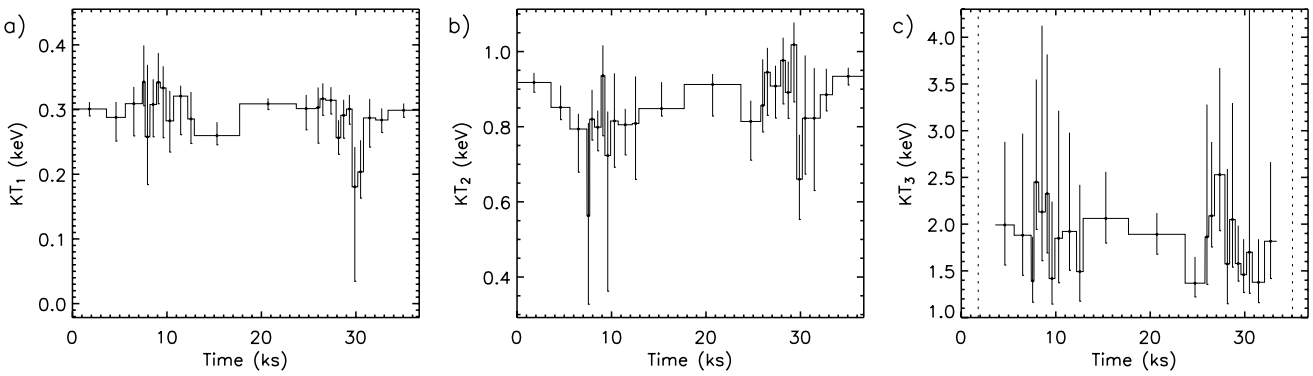

Fig. 7. Time-evolution of the coronal temperatures obtained with the 3-T model. In the KT_3 panel, a dashed line marks the time-segments for which this temperature could not be constrained (see text). Note that the time-resolution is the same as that shown in Fig. 5.

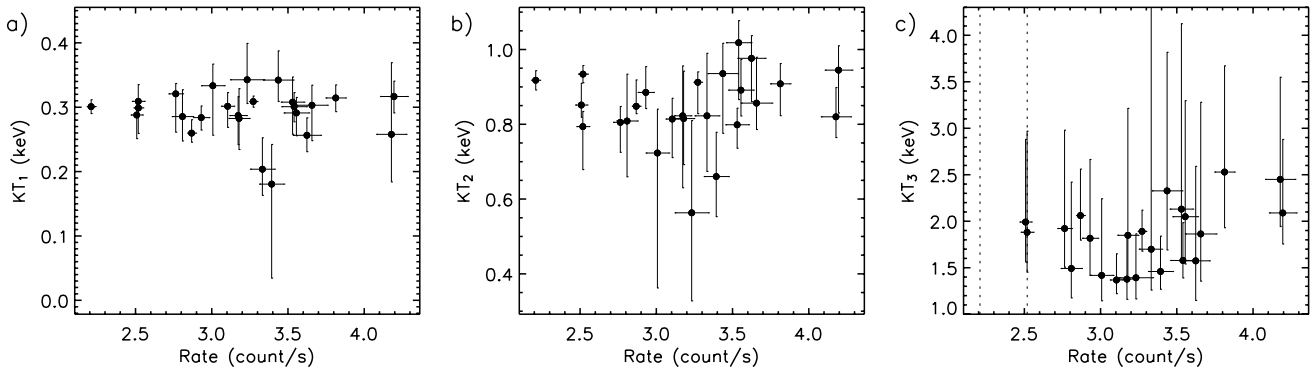

Fig. 8. Coronal temperatures (obtained with the 3-T model) vs. count-rate. In the KT_3 panel, a dashed line marks the time-segments for which this temperature could not be constrained (see text). Note that no significant changes in the temperature values are observed even at flare maxima (points with the highest count-rates).

stellar flares. They found that synthesized stellar-like spectra of solar flares (previously subtracted by the quiescent "background" spectrum) are generally well-fitted with a single thermal component (1-T model) at a temperature close to that of the maximum of the $EM(T)$ distribution. However, two thermal components are sometimes needed to fit the data during the decay, probably due to a rapid variation of the plasma temperature within this phase. In fact, they detected deviations from the isothermal description for the flares with no significant sustained heating. Consequently, our first approach consisted on using a 3-T model to fit each observed spectrum, fixing all the parameters of the first two components at their quiescent values, whereas the temperature and emission measure of the third component (which describes the flaring plasma) were free to vary. Generally, the statistics did not allow to constrain the abundance of the additional APEC component. Therefore, it was assumed to be equal to the global abundance obtained for the quiescent state in order to avoid unphysical solutions. Results showed that this model failed to reproduce the observed data under the considered assumptions. A systematic excess at high energies appeared in the residuals, and the temperature of the hottest component resulted to be very similar to that of the second one. This suggested us that the emission measure of the second component may be changing (note that we fixed it at its quiescent value), and therefore the third component was trying to compensate its enhancement providing a temperature lower than that required to fit the high-energy region of the spectra. For these reasons, we decided to perform a self-consistent analysis by fitting the data using an "iterative" procedure, which is described below.

Each spectrum was fitted with a 3-T model, taking the same global abundance for all the thermal components and fixing it at its quiescent value. The first iteration was done leaving all the temperatures and emission measures as free parameters. Results for the temperature of the coolest component (KT_1) were plotted versus time (Fig. 7a) and count-rate (Fig. 8a). No change in KT_1 was noticed. Moreover, the normalized histogram of the time-weighted values of KT_1 (Fig. 9a) showed an approximately Gaussian distribution peaked at the temperature of the coolest component of the 2-T model that described the quiescent state. A Gaussian fit provided the mean temperature of the distribution, together with its uncertainty (standard deviation), that is

$$\overline{KT}_1 = 0.296 \pm 0.016 \text{ keV}.$$

This value can be considered the best estimation for the temperature of the coolest component. Since $\overline{KT}_1$ was constant during the observation, we fixed it and computed the fits again (second iteration) allowing variations in the other two temperatures and in the emission measure of all the three thermal components. No change was then detected in KT_2 (see Figs. 7b and 8b). This temperature also appeared to be uniform throughout the observation. Using a Gaussian distribution to fit the normalized histogram of the time-weighted values of this parameter (Fig. 9b), we obtained

$$\overline{KT}_2 = 0.88 \pm 0.06 \text{ keV},$$

which is clearly consistent with the temperature of the hottest component of the 2-T model that described the quiescent state.

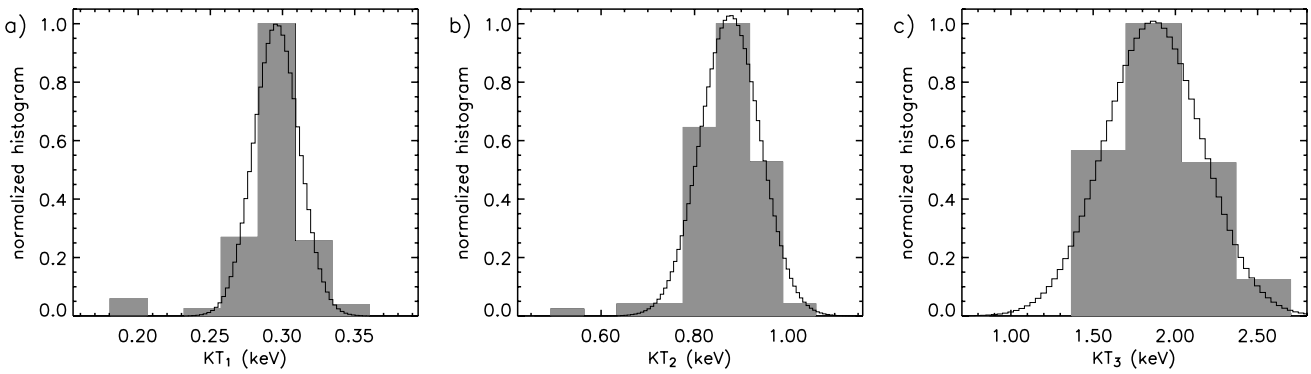

Fig. 9. Distribution of the three temperatures that characterize the corona of CC Eri during the XMM-Newton observation. The corresponding Gaussian fits are also plotted.

In addition to $\overline{KT}_1$, $\overline{KT}_2$ was also fixed in the model and the fits were repeated (third iteration) leaving free the temperature of the hottest component and the three emission measures. Figures 7c and 8c show the values obtained for KT_3 versus time and count-rate, respectively. It was not possible to constrain this temperature for the segments with an emission level equal or very similar to that of the quiescent state (first and last time-intervals). However, we cannot discard the existence of a little amount of hotter material during these time-intervals, with a contribution not strong enough to be detected. No clear pattern was detected in the time-evolution of KT_3 during the observed flares (see Fig. 7c). In fact, the most surprising result is that no significant enhancement in this temperature was found during any phase of the observed flares when comparing them with non-flaring intervals (see also Fig. 8c). Furthermore, when accounting for the calculated uncertainties, all the values of KT_3 are compatible with the average value obtained by fitting a Gaussian distribution to the normalized histogram of the time-weighted values of KT_3 (Fig. 9c), as occurred for the other two temperatures, that is

$$\overline{KT}_3 = 1.87 \pm 0.30 \text{ keV}.$$

Therefore, we fixed the three temperatures ($\overline{KT}_1$, $\overline{KT}_2$ and $\overline{KT}_3$) and computed the last iteration leaving all the emission measures as free parameters when doing the fits. Results of the best-fitting models are given in Table 3 (note that the first and last time-intervals were also fitted with the same model). All the calculated fits can be considered good-quality models in terms of the $\chi^2_{\rm red}$ test statistic. The time-evolution of the three emission measures is plotted in Fig. 10. Figure 11 complements this figure giving the emission measure of each component versus the count-rate.

Our analysis shows that the occurrence of flares may be explained with the increasing of the emission measures related to the hottest temperatures, and in particular to the third one, while the dominant temperatures remain unchanged.

4.2. Loop modeling

Although stellar flares are not spatially resolved, we can infer the size of these structures by assuming that they are produced by the same basic physical mechanisms as solar flares and using flare loop models (see Kopp & Poletto 1984; White et al. 1986; Poletto et al. 1988; van den Oord & Mewe 1989; Pallavicini et al. 1990; Serio et al. 1991; Hawley et al. 1995; Reale et al. 1997; or the review given by Reale 2002, for an extensive discussion and comparison of these methods). Under the hypothesis of flares occurring inside closed coronal structures, and assuming that the heat pulse is released at the beginning of the flare, the decay time of the X-ray emission scales with the length of the loop which confines the flaring plasma. However, the presence of significant heating during the decay would slow down this phase and, therefore, the size of the flaring loop would be overestimated. It was shown that the slope (ζ) of the path of the flare decay in the density-temperature ($\log n_{\rm F} - \log T_{\rm F}$) plane mainly depends on the heating decay time (Jakimiec et al. 1992; Sylwester et al. 1993; Reale et al. 1997). Reale et al. (1997) derived an empirical formula using hydrodynamic simulations of single semi-circular flaring loops with constant cross-section, and including the effect of the heating in the decay:

$$L = \frac{\tau_D \sqrt{T_{\rm max}}}{3.7 \times 10^{-4} F(\zeta)} \qquad F(\zeta) \geq 1 \tag{2}$$

where L is the loop half-length (in cm), $T_{\rm max}$ the loop maximum temperature (in K), τ_D the e-folding decay time derived from the light curve (in seconds), and $F(\zeta)$ a non-dimensional factor (larger than one) which accounts for the heating in the decay. The slope of the decay path in the density-temperature diagram is maximum (~2) if the heating is negligible during the decay, and minimum (~0.5) if the heating dominates this phase (Jakimiec et al. 1992). Equation (2) was successfully tested on resolved solar flares observed with Yohkoh/SXT (Reale et al. 1997) and has been further extended and applied to several stellar flares observed with a wide variety of detectors (Reale & Micela 1998; Favata et al. 2000a,b,c, 2001; Maggio et al. 2000; Güdel et al. 2001; Stelzer et al. 2002; Briggs & Pye 2003; Reale et al. 2004; Pillitteri et al. 2005; Franciosini et al. 2006). The correction factor $F(\zeta)$ needs to be calibrated for each detector, since it depends on the spectral bandpass and resolution. For EPIC-PN observations, the expression given by Reale (2007) has to be used:

$$F(\zeta) = \frac{c_a}{\zeta - \zeta_a} + q_a \tag{3}$$

where $c_a = 0.51$, $\zeta_a = 0.35$, $q_a = 1.36$. Equation (3) can be used for slopes in the range $0.35 < \zeta \leq 1.6$.

For stellar flares the density can rarely be directly measured. Nevertheless, since reasonably the soft X-ray flare volume is approximately constant during the flare development, the square root of the emission measure can be used as a proxy for the density (note that $EM_{\rm F} = \int n_{\rm e} n_{\rm H} \, {\rm d}V_{\rm F} \approx n_{\rm F}^2 V_{\rm F}$ for a totally ionized hydrogen plasma).

As described in Sect. 4.1, the analysed flares (FB and FC) only involve the two hottest components of the 3-T model used

Table 3. Results derived from the time-resolved spectral analysis after fixing the hydrogen column density, the global coronal abundance, and the different temperatures (see text in Sect. 4.1). Columns show: (1) label referring to the time-region where the spectrum is included (see Figs. 1 and 5); (2) time-coverage; (3)–(5) emission measures, from the coolest (EM_1) to the hottest (EM_3) thermal components; (6) reduced χ^2 and degrees of freedom; (7) and (8) X-ray flux and luminosity in the 0.5–10.0 keV band.

(1)Region	(2)Time$_{start}$ – Time$_{end}$ (ks)	(3)EM_1 (10^{52} cm^{-3})	(4)EM_2 (10^{52} cm^{-3})	(5)EM_3 (10^{52} cm^{-3})	(6)χ^2_{red} (d.o.f)	(7)f_X (10^{-11} erg cm^{-2} s^{-1})	(8)log L_X(erg s^{-1})
L0	0.0–3.6	$1.63^{+0.09}_{-0.09}$	$1.43^{+0.08}_{-0.08}$	$0.10^{+0.08}_{-0.08}$	1.44 (150)	1.52	29.38
FA	3.6–5.6	$1.58^{+0.13}_{-0.13}$	$1.58^{+0.12}_{-0.12}$	$0.42^{+0.11}_{-0.11}$	1.11 (209)	1.77	29.45
FB	5.6–7.4	$1.67^{+0.14}_{-0.14}$	$1.54^{+0.12}_{-0.12}$	$0.42^{+0.12}_{-0.12}$	0.97 (200)	1.78	29.45
FB	7.4–7.7	$1.92^{+0.38}_{-0.37}$	$1.69^{+0.37}_{-0.35}$	$1.17^{+0.41}_{-0.39}$	0.96 (85)	2.39	29.58
FB	7.7–8.2	$1.55^{+0.32}_{-0.31}$	$2.33^{+0.31}_{-0.30}$	$2.05^{+0.34}_{-0.35}$	0.87 (161)	3.17	29.70
FB	8.2–8.9	$2.00^{+0.26}_{-0.25}$	$2.13^{+0.24}_{-0.24}$	$0.92^{+0.25}_{-0.24}$	0.97 (98)	2.55	29.61
FB	8.9– 9.3	$1.60^{+0.33}_{-0.32}$	$1.76^{+0.31}_{-0.30}$	$1.65^{+0.36}_{-0.35}$	1.02 (111)	2.61	29.62
FB	9.3–9.9	$1.81^{+0.26}_{-0.25}$	$1.97^{+0.24}_{-0.24}$	$0.50^{+0.25}_{-0.23}$	0.89 (114)	2.14	29.53
FB	9.9–10.7	$1.95^{+0.23}_{-0.22}$	$1.92^{+0.21}_{-0.21}$	$0.70^{+0.22}_{-0.21}$	1.21 (166)	2.27	29.56
FB	10.7–12.2	$1.71^{+0.16}_{-0.15}$	$1.64^{+0.14}_{-0.14}$	$0.63^{+0.15}_{-0.14}$	1.19 (200)	1.98	29.50
FB	12.2–12.9	$1.95^{+0.23}_{-0.23}$	$1.61^{+0.22}_{-0.21}$	$0.54^{+0.23}_{-0.22}$	0.95 (147)	1.99	29.50
L1	12.9–17.7	$1.78^{+0.09}_{-0.09}$	$1.67^{+0.08}_{-0.08}$	$0.69^{+0.09}_{-0.09}$	1.22 (275)	2.06	29.51
L2	17.7–23.7	$1.81^{+0.08}_{-0.08}$	$1.94^{+0.08}_{-0.08}$	$0.92^{+0.09}_{-0.09}$	1.06 (264)	2.37	29.57
FC	23.7–25.8	$1.89^{+0.14}_{-0.14}$	$1.98^{+0.13}_{-0.13}$	$0.55^{+0.14}_{-0.14}$	1.36 (234)	2.20	29.54
FC	25.8–26.2	$2.12^{+0.35}_{-0.33}$	$2.22^{+0.31}_{-0.32}$	$0.91^{+0.33}_{-0.32}$	0.99 (121)	2.64	29.62
FC	26.2–26.8	$2.12^{+0.30}_{-0.29}$	$2.07^{+0.27}_{-0.27}$	$1.95^{+0.31}_{-0.30}$	1.12 (175)	3.16	29.70
FC	26.8–27.9	$1.86^{+0.21}_{-0.21}$	$2.14^{+0.21}_{-0.20}$	$1.44^{+0.23}_{-0.23}$	1.12 (184)	2.81	29.65
FC	27.9–28.4	$1.95^{+0.30}_{-0.29}$	$2.15^{+0.29}_{-0.28}$	$1.08^{+0.32}_{-0.30}$	0.91 (142)	2.64	29.62
FC	28.4–29.0	$2.33^{+0.28}_{-0.27}$	$1.91^{+0.25}_{-0.25}$	$1.00^{+0.27}_{-0.26}$	0.82 (155)	2.57	29.61
FC	29.0–29.6	$2.21^{+0.28}_{-0.27}$	$1.62^{+0.25}_{-0.25}$	$1.47^{+0.28}_{-0.27}$	1.19 (160)	2.63	29.62
FC	29.6–30.2	$1.89^{+0.28}_{-0.27}$	$1.98^{+0.27}_{-0.26}$	$0.99^{+0.28}_{-0.27}$	0.99 (156)	2.47	29.59
FC	30.2–30.8	$2.00^{+0.27}_{-0.27}$	$2.07^{+0.26}_{-0.25}$	$0.69^{+0.27}_{-0.26}$	0.96 (149)	2.38	29.58
FC	30.8–32.1	$2.15^{+0.19}_{-0.19}$	$1.90^{+0.18}_{-0.17}$	$0.54^{+0.18}_{-0.17}$	1.05 (148)	2.24	29.55
FC	32.1–33.4	$2.00^{+0.17}_{-0.17}$	$1.73^{+0.16}_{-0.15}$	$0.53^{+0.16}_{-0.15}$	1.15 (190)	2.08	29.52
FC	33.4–36.7	$1.82^{+0.10}_{-0.10}$	$1.67^{+0.09}_{-0.09}$	$0.12^{+0.09}_{-0.09}$	1.73 (139)	1.74	29.44

to fit the spectra. We obtained the flare contribution of each one of these components to the total emission measure ($EM_{2,F}$ and $EM_{3,F}$) by simply subtracting from EM_2 and EM_3 their corresponding value measured for the quiescent state (L0). Therefore, the total emission measure of the flaring plasma (EM_F) is given by the sum of $EM_{2,F}$ and $EM_{3,F}$. A mean temperature of the flaring plasma (T_F) was also calculated for each spectrum as a weighted average of the temperature of the two hottest components in the 3-T model, where the respective weights were $EM_{2,F}/EM_F$ and $EM_{3,F}/EM_F$. The resulting log $EM_F^{1/2}$–log T_F diagram is plotted in Fig. 12 for the decay of FB and FC. A linear fit to the data provided a slope of $\zeta = 0.18 \pm 0.27$ for FB and $\zeta = 0.45 \pm 0.08$ for FC, indicating the presence of sustained heating during the decay of both flares. Since the slope for FB is compatible with the lower asymptotic value for which Eq. (3) can be applied, we obtained an upper limit for the loop half-length of this flare by using $\zeta = 0.45$. The maximum temperature in the flaring loop (T_{max}) can be derived from the maximum observed temperature ($T_{F,max}$). The observed temperature is a kind of average temperature of the flaring loop, which is therefore lower than the loop maximum temperature. The relationship between T_{max} and $T_{F,max}$ depends on the instrumental response. For EPIC-PN, Reale et al. (2004) reported:

$$T_{max} = 0.184 T_{F,max}^{1.130}. \quad (4)$$

Thus, T_{max} resulted to be 32×10^6 K for FB, and 30×10^6 K for FC, with uncertainties of 16%.

Using the quantities given above, the values of τ_D shown in Table 2, and Eqs. (2) and (3), we obtained $L < 7 \times 10^9$ cm for the half-length of the loop involved in the flare FB, and $L \approx (14 \pm 8) \times 10^9$ cm for that involved in FC.

5. Discussion and conclusions

We have presented a detailed study of the X-ray variability that the binary star CC Eri showed during an XMM-Newton observation. The great sensitivity of the EPIC-PN CCD camera allowed us to perform time-resolved spectroscopy of two flares weaker (flux increases of factors 1.5–1.9) than those typically analysed in the literature. The maximum luminosity of these flares in the 0.5–10.0 keV band was $\approx 2.6 \times 10^{29}$ erg/s.

Results show that, during the analysed observation, the corona of CC Eri is well-described by a 3-T model with constant temperatures (values of 3, 10 and 22 MK) and time-variable emission measures. The emission measure of the coolest component (EM_1) ranges between 1.6–2.3×10^{52} cm^{-3}, the one of the second component (EM_2) between 1.4–2.3×10^{52} cm^{-3}, and that of the hottest component (EM_3) varies between 0.1–2.1×10^{52} cm^{-3}. That is, EM_1 reaches 1.4 times the value measured

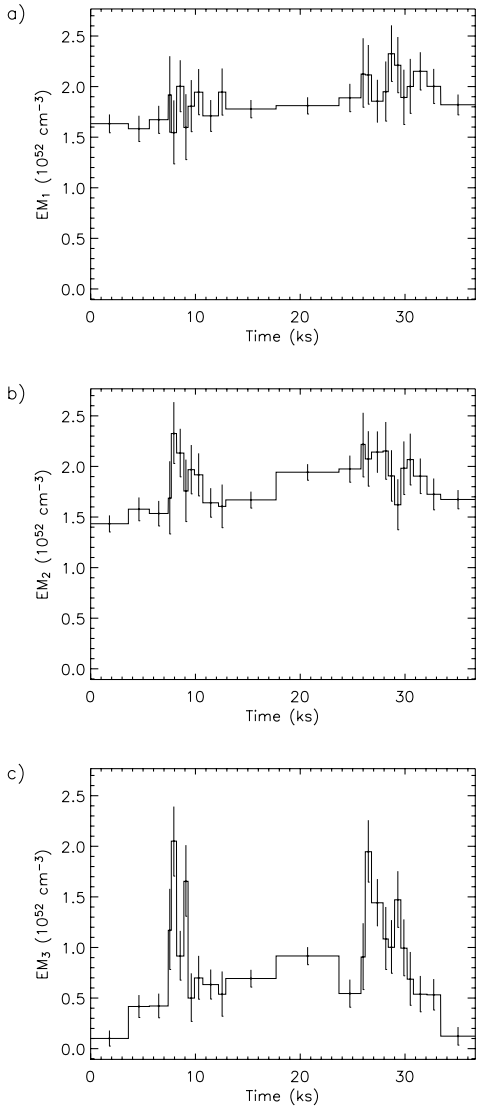

Fig. 10. Time-evolution obtained for the emission measure of the three thermal components. Note that the time-resolution is the same as that shown in Fig. 5.

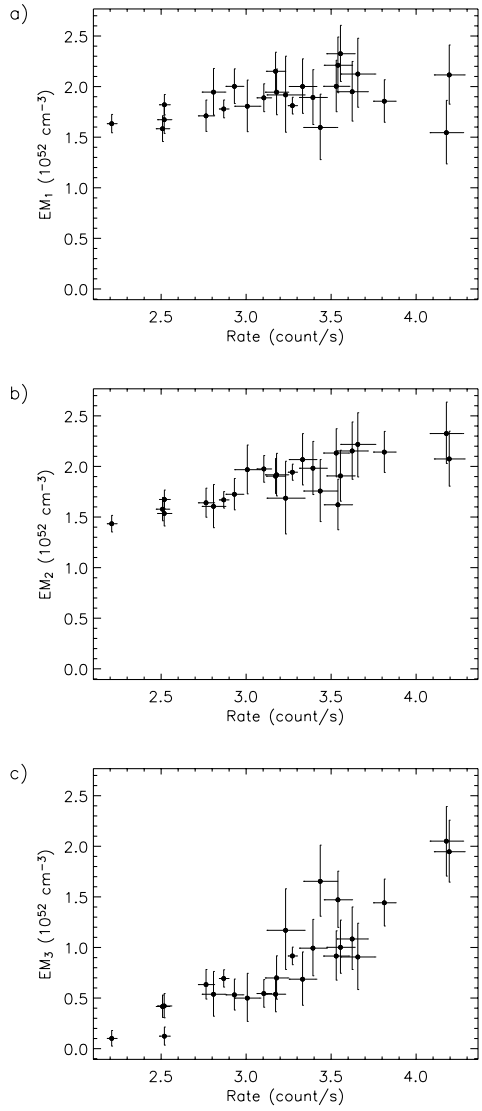

Fig. 11. Emission measure of the three thermal components vs. count-rate.

for the quiescent state, EM_2 varies up to a factor of 1.6, and EM_3 increases up to 21 times its quiescent value. Therefore, the hottest component dominates the X-ray variability observed on CC Eri (see also Fig. 10). The changes in the emission measure of the coolest component could be due to the variable aspect of the binary during its orbital motion. However, the changes in the emission measure of the two hottest components are clearly correlated with the variations observed in the light curve during the detected flares (see Figs. 10 and 11). The results obtained for the two hottest components resemble those reported by Reale et al. (2001) for a sample of solar flares that covered a wide range of intensities and physical conditions. They found that the $EM(T)$ distribution of all the flares in the sample follows a common evolution path: it starts low but already at a relatively high temperature ($\sim 10^7$ K independently of the flare intensity), it grows toward higher EM values during the rising phase and then decreases during the decay, maintaining always a more or less constant shape and peak temperature. In other words, they found that the height of the $EM(T)$ distribution is clearly variable during the different phases of solar flares, while the width and peak temperature of the distribution suffer from much smaller changes. As far as we are concerned, this is the first time that no evident temperature variations are observed in a time-resolved study of stellar flares (see Figs. 7 and 8). Besides, the fact that the temperatures that characterize the flaring plasma coincide with those of the quiescent state is consistent with a recurrent idea in the literature, that is: the quiescent emission of magnetically active stars may be produced, to a large fraction, by continuous flaring activity (see Sect. 1 and references therein). Thus, the light curves of multiple small flares overlap, and only larger flares stand out from the quiescent level. Besides, without temperature variations, differences in the emission measure between time-intervals with diverse count-rate, such as those observed for L0, L1 and L2 (see Fig. 1 and Table 3), can be identified with differences in the total coronal volume occupied by the flaring plasma. Density variations may also account for the changes in emission measure. However, we expect that, if they were significant, they would be driven by local heating injections or leaks, and therefore coupled to temperature variations but, as discussed above, temperature variations are not detected.

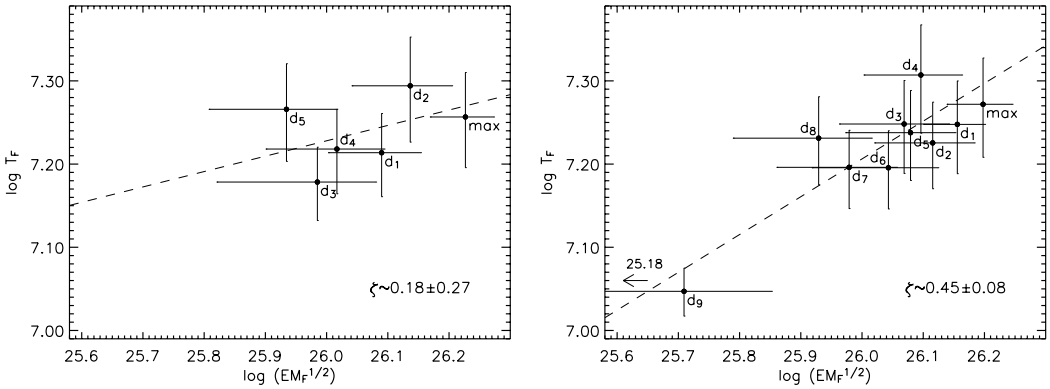

Fig. 12. Density-temperature ($\log n_F - \log T_F$) diagram of the variable component (see text) for the decay phase of flares FB (*left panel*) and FC (*right panel*). $EM_F^{1/2}$ has been used as a proxy for the density. Numbers indicate the time-evolution of the values. The point at the flare maximum (max) is also plotted. For each flare, the dashed line shows the best linear fit to the decay data. The derived slopes (ζ) are also given.

The slope of the path in the density-temperature diagram indicates the presence of significant heating during the decay of the analysed flares, and leads to an upper limit of 7 and 14×10^9 cm, respectively, for the half-length of the flaring loops. From the orbital solution of CC Eri (Amado et al. 2000) and the stellar radius of its components, we obtain a minimum distance between their surfaces of $\sim 1.4 \times 10^{11}$ cm. Even the largest loops involved in the detected flares only cover ~10% of this distance. Therefore, it is likely that the flaring loops are included all in the corona of one of the stars, and do not result from the magnetic fields bridging the two stars. In addition, bearing the spectral type of the stellar components of CC Eri in mind, the ratio between the half-length of the flaring loops and the stellar radius (R_*) would be 0.1 and 0.3 if the flares were produced by the K7.5Ve star, or 0.2 and 0.4 if they were produced by the M3.5Ve star. In both cases, the loop height above the stellar surface ($2L/\pi$ for vertical loops with semi-circular geometry) is about $0.1-0.3\ R_*$, implying a relatively compact flaring corona. These results are in agreement with the loop half-lengths derived for other Me dwarfs ($L \leq 0.5\ R_*$; Favata & Micela 2003).

Assuming that at the flare peak the flaring loop is not far from a steady-state condition, and given that the derived loop half-lengths are significantly smaller than the pressure scale height[2], we can apply the so-called RTV scaling laws (Rosner et al. 1978). These relationships link the pressure (p) and the heating rate per unit volume (E_H) with the loop half-length and the loop maximum temperature. Table 4 lists all these quantities for the observed flares. We have also estimated the electron density under the assumption of a totally ionized hydrogen plasma, obtaining $n_e \sim 10^{11}$ cm^{-3}. This is compatible with values expected for a plasma in coronal conditions. In order for the electron density to be consistent with the EM_F measured at the peak of the analysed flares, the flaring volumes should be as large as 10^{30} cm^3. From the pressure of the flaring plasma (see Table 4), we infer that the minimum magnetic field required to confine the plasma at the flare peak is ~210 G for FB and ~140 G for FC.

To satisfy the energy balance relation for the flaring region as a whole, the maximum X-ray luminosity must be lower than the total input energy rate at the flare peak ($H = E_H V_F$). The rest of the input energy is used for thermal conduction, kinetic energy and radiation at lower frequencies. From the analysis of a large optical flare on the M3.5Ve star AD Leo, Houdebine et al. (1993) concluded that the total kinetic energy during the event was of the same order as the radiated energy. For both FB and FC, we obtain that $L_{X,max}$ is about 10% of H, compatible with the X-ray radiation being only one of the energy loss terms during the detected flares. This value is in agreement with those reported for solar flares, where the soft X-ray radiation at the peak only accounts for 10−20% of the total energy budget (Wu et al. 1986). Reale et al. (2004) found a similar percentage (~15%) for a flare observed on the M5.5Ve star Proxima Centauri, while Favata et al. (2000c) estimated a higher value (~35%) for an extreme X-ray flare detected on the M3.5Ve star EV Lac.

If the detected flares were produced by a single loop, its aspect ($\beta = r/L$, where r is the radius of the loop cross-section derived from the volume and loop length) should be 0.6 for

Table 4. Parameters derived for flares FB and FC.

	Flare FB	Flare FC
[a] τ_D (s)	2850	5960
[b] $L_{X,max}$ (10^{29} erg s^{-1})	2.6	2.6
[c] $E_{X,tot}$ (10^{33} erg)	0.75	1.5
[d] ζ	0.18 ± 0.27	0.45 ± 0.08
[e] T_{max} (10^6 K)	32 ± 5	30 ± 5
[f] L (10^9 cm)	<7	14 ± 8
[g] p (10^3 dyn cm^{-2})	>1.7	0.74 ± 0.34
[h] n_e (10^{11} cm^{-3})	>2.0	0.88 ± 0.43
[i] V_F (10^{30} cm^3)	<0.7	3.2
[j] E_H (erg s^{-1} cm^{-3})	>3.7	~0.8
[k] N_{loops}	~38	~19
[l] B (G)	>210	>140

[a] e-folding decay time derived from the light curve. [b] Luminosity at the flare peak (0.5−10.0 keV band). [c] Total radiated energy (0.5−10.0 keV band). [d] Slope of the decay path in the density-temperature diagram (see details in Sect. 4.2). [e] Maximum temperature in the loop at the flare peak (see Sect. 4.2). [f] Half-length of the flaring loops (see Sect. 4.2). [g] Maximum pressure in the loop at the flare peak (estimated from the loop scaling laws given by Rosner et al. 1978). [h] Maximum electron density in the loop at the flare peak. We have assumed a totally ionized hydrogen plasma (i.e., $p = 2n_e kT_{max}$). [i] Volume of the flaring region (note that $EM_F \approx n_e^2 V_F$ for a totally ionized hydrogen plasma). [j] Heating rate per unit volume at the flare peak (estimated from the loop scaling laws given by Rosner et al. 1978). [k] Number of loops needed to fill the flare volume. We have assumed a loop aspect $r/L = 0.1$ for a single loop. [l] Magnetic field ($p \leq p_B = B^2/8\pi$).

[2] The pressure scale height is defined as $h_p = 2kT_{max}/(\mu g)$, where μ is the average atomic weight and g is the surface gravity of the star. Therefore, $h_p \approx 5000 T_{max}/(g/g_\odot)$. Taking the spectral type of the stellar components of CC Eri into account, $h_p \geq 7 \times 10^{10}$ cm for both FB and FC.

FB and 0.4 for FC. Such a large cross-section is not observed on solar coronal loops, for which typical values of β are in the range 0.1−0.3. Therefore, we suggest a more realistic scenario consisting on flaring structures made up of several similar loops. Assuming $\beta = 0.1$, FB and FC occur in arcades composed of ∼38 and 19 loops, respectively. Similar structures are also observed to flare on the Sun. For example, the Bastille day flare (2000 July 14) is an intense solar flare (GOES class X6) that occurred on a curved arcade with some 100 post-flare loops (Aschwanden & Alexander 2001; Reeves & Warren 2002). Stellar analogues have been proposed for the Me dwarf Proxima Centauri, where the best description for a flare analysed by Reale et al. (2004) shows the presence of an arcade made up of ∼5 loops; and also for the younger (∼100 Myr) G9 dwarf ZS 76, where Pillitteri et al. (2005) estimated 20−30 loops for the flaring arcades. Therefore, we conclude that events like solar arcade flares may be a common phenomenon on stars, in wide generality.

Acknowledgements. I.C.C. acknowledges support from the Spanish Ministerio de Educación y Ciencia (MEC), under the grant AP2001-0475 (programa nacional de Formación de Profesorado Universitario) and project AYA2005-02750 (Programa Nacional de Astronomía y Astrofísica). The work of J.L.S. has been supported by the Marie Curie Fellowship Contract No. MTKD-CT-2004-002769. We thank John Pye for useful comments which have contributed to improve the manuscript.

References

Amado, P. J., Doyle, J. G., Byrne, P. B., et al. 2000, A&A, 359, 159
Anders, E., & Grevesse, N. 1989, Geochim. Cosmochim. Acta, 53, 197
Arnaud, K. 1996, Astronomical Data Analysis Software and Systems V, ASP Conf. Ser., 101, 17
Arnaud, K. 2004, AAS/High Energy Astrophysics Division, 8, #16.29
Aschwanden, M. J., & Alexander, D. 2001, Sol. Phys., 204, 91
Aschwanden, M. J., Tarbell, T. D., Nightingale, R. W., et al. 2000, ApJ, 535, 1047
Audard, M., Güdel, M., & Guinan, E. F. 1999, ApJ, 513, L53
Audard, M., Güdel, M., Drake, J. J., & Kashyap, V. L. 2000, ApJ, 541, 396
Bopp, B. W., & Evans, D. S. 1973, MNRAS, 164, 343
Bopp, B. W., & Fekel, F., Jr. 1977, AJ, 82, 490
Briggs, K. R., & Pye, J. P. 2003, MNRAS, 345, 714
Busko, I. C., & Torres, C. A. O. 1976, Informational Bulletin on Variable Stars, 1186, 1
Busko, I. C., & Torres, C. A. O. 1978, A&A, 64, 153
Busko, I. C., Quast, G. R., & Torres, C. A. O. 1977, A&A, 60, L27
Byrne, P. B., Agnew, D. J., Cutispoto, G., et al. 1992, Surface Inhomogeneities on Late-Type Stars, LNP, 397, 255
Caillault, J.-P. 1982, AJ, 87, 558
Caillault, J.-P., Drake, S., & Florkowski, D. 1988, AJ, 95, 887
Collura, A., Pasquini, L., & Schmitt, J. H. M. M. 1988, A&A, 205, 197
Crosby, N. B., Aschwanden, M. J., & Dennis, B. R. 1993, Sol. Phys., 143, 275
Datlowe, D. W., Elcan, M. J., & Hudson, H. S. 1974, Sol. Phys., 39, 155
Dennis, B. R. 1985, Sol. Phys., 100, 465
Demircan, O., Eker, Z., Karataş, Y., & Bilir, S. 2006, MNRAS, 366, 1511
Ehle, M., Pollock, A. M. T., Talavera, A., et al. 2004, User's Guide to the XMM-Newton Science Analysis System
Evans, D. S. 1959, MNRAS, 119, 526
Favata, F., & Micela, G. 2003, Space Sci. Rev., 108, 577
Favata, F., Micela, G., & Reale, F. 2000a, A&A, 354, 1021
Favata, F., Micela, G., Reale, F., Sciortino, S., & Schmitt, J. H. M. M. 2000b, A&A, 362, 628
Favata, F., Reale, F., Micela, G., et al. 2000c, A&A, 353, 987
Favata, F., Micela, G., & Reale, F. 2001, A&A, 375, 485
Franciosini, E., Pillitteri, I., Stelzer, B., et al. 2006, [arXiv:astro-ph/0611632]
Güdel, M. 1992, A&A, 264, L31
Güdel, M. 2004, A&ARv, 12, 71
Güdel, M., Audard, M., Briggs, K., et al. 2001, A&A, 365, L336
Güdel, M., Audard, M., Kashyap, V. L., Drake, J. J., & Guinan, E. F. 2003, ApJ, 582, 423
Güdel, M., Audard, M., Reale, F., Skinner, S. L., & Linsky, J. L. 2004, A&A, 416, 713
Haisch, B. M. 1983, ASSL, IAU Colloq. 71: Activity in Red-Dwarf Stars, 102, 255
Hawley, S. L., Fisher, G. H., Simon, T., et al. 1995, ApJ, 453, 464
Houdebine, E. R., Foing, B. H., Doyle, J. G., & Rodono, M. 1993, A&A, 278, 109
Hudson, H. S. 1991, Sol. Phys., 133, 357
Jakimiec, J., Sylwester, B., Sylwester, J., et al. 1992, A&A, 253, 269
Kashyap, V. L., Drake, J. J., Güdel, M., & Audard, M. 2002, ApJ, 580, 1118
Katsova, M. M., Livshits, M. A., & Schmitt, J. H. M. M. 2002, Stellar Coronae in the Chandra and XMM-NEWTON Era, ASP Conf. Ser., 277, 515
Kopp, R. A., & Pneuman, G. W. 1976, Sol. Phys., 50, 85
Kopp, R. A., & Poletto, G. 1984, Sol. Phys., 93, 351
Krucker, S., & Benz, A. O. 1998, ApJ, 501, L213
Lin, R. P., Schwartz, R. A., Kane, S. R., Pelling, R. M., & Hurley, K. C. 1984, ApJ, 283, 421
Maggio, A., Pallavicini, R., Reale, F., & Tagliaferri, G. 2000, A&A, 356, 627
Marino, A., Micela, G., & Peres, G. 2000, A&A, 353, 177
Mitra-Kraev, U., Harra, L. K., Güdel, M., et al. 2005, A&A, 431, 679
Morrison, R., & McCammon, D. 1983, ApJ, 270, 119
Nousek, J. A., & Shue, D. R. 1989, ApJ, 342, 1207
Osten, R. A., & Brown, A. 1999, ApJ, 515, 746
Osten, R. A., Brown, A., Wood, B. E., & Brady, P. 2002, ApJS, 138, 99
Pace, G., & Pasquini, L. 2004, A&A, 426, 1021
Pallavicini, R. 1988, Mem. Soc. Astron. Ital., 59, 71
Pallavicini, R., Serio, S., & Vaiana, G. S. 1977, ApJ, 216, 108
Pallavicini, R., Golub, L., Rosner, R., et al. 1981, ApJ, 248, 279
Pallavicini, R., Monsignori-Fossi, B. C., Landini, M., & Schmitt, J. H. M. M. 1988, A&A, 191, 109
Pallavicini, R., Tagliaferri, G., & Stella, L. 1990, A&A, 228, 403
Pan, H. C., & Jordan, C. 1995, MNRAS, 272, 11
Parker, E. N. 1975, ApJ, 198, 205
Perryman, M. A. C., Lindegren, L., Kovalevsky, J., et al. 1997, A&A, 323, L49
Pettersen, B. R. 1991, Mem. Soc. Astron. Ital., 62, 217
Pillitteri, I., Micela, G., Reale, F., & Sciortino, S. 2005, A&A, 430, 155
Poletto, G., Pallavicini, R., & Kopp, R. A. 1988, A&A, 201, 93
Porter, J. G., Fontenla, J. M., & Simnett, G. M. 1995, ApJ, 438, 472
Priest, E. R. 1981, Solar Flare Magnetohydrodynamics, 1
Reale, F. 2002, Stellar Coronae in the Chandra and XMM-NEWTON Era, ASP Conf. Ser., 277, 103
Reale, F. 2007, A&A, submitted
Reale, F., & Micela, G. 1998, A&A, 334, 1028
Reale, F., Serio, S., & Peres, G. 1993, A&A, 272, 486
Reale, F., Betta, R., Peres, G., Serio, S., & McTiernan, J. 1997, A&A, 325, 782
Reale, F., Peres, G., & Orlando, S. 2001, ApJ, 557, 906
Reale, F., Güdel, M., Peres, G., & Audard, M. 2004, A&A, 416, 733
Reeves, K. K., & Warren, H. P. 2002, ApJ, 578, 590
Rengarajan, T. N. 1984, ApJ, 283, L63
Robrade, J., & Schmitt, J. H. M. M. 2005, A&A, 435, 1073
Rosner, R., Tucker, W. H., & Vaiana, G. S. 1978, ApJ, 220, 643
Serio, S., Reale, F., Jakimiec, J., Sylwester, B., & Sylwester, J. 1991, A&A, 241, 197
Schmitt, J. H. M. M. 1997, A&A, 318, 215
Schmitt, J. H. M. M., Collura, A., Sciortino, S., et al. 1990, ApJ, 365, 704
Schmitt, J. H. M. M., Fleming, T. A., & Giampapa, M. S. 1995, ApJ, 450, 392
Slee, O. B., Budding, E., Carter, B. D., et al. 2004, PASA, 21, 72
Smith, R. K., Brickhouse, N. S., Liedahl, D. A., & Raymond, J. C. 2001a, ApJ, 556, L91
Smith, R. K., Brickhouse, N. S., Liedahl, D. A., & Raymond, J. C. 2001b, ASP Conf. Ser.: Spectroscopic Challenges of Photoionized Plasmas, 247, 161
Smith, K., Güdel, M., & Audard, M. 2005, A&A, 436, 241
Stelzer, B., Burwitz, V., Audard, M., et al. 2002, A&A, 392, 585
Strassmeier, K. G., Hall, D. S., Fekel, F. C., & Scheck, M. 1993, A&AS, 100, 173
Strüder, L., Briel, U., Dennerl, K., et al. 2001, A&A, 365, L18
Sylwester, B., Sylwester, J., Serio, S., et al. 1993, A&A, 267, 586
Tsikoudi, V. 1982, ApJ, 262, 263
Turner, M. J. L., Abbey, A., Arnaud, M., et al. 2001, A&A, 365, L27
van den Besselaar, E. J. M., Raassen, A. J. J., Mewe, R., et al. 2003, A&A, 411, 587
van den Oord, G. H. J., & Mewe, R. 1989, A&A, 213, 245
Vilhu, O. 1984, A&A, 133, 117
Vilhu, O., & Walter, F. M. 1987, ApJ, 321, 958
Walter, F. M. 1982, ApJ, 253, 745
White, N. E., Culhane, J. L., Parmar, A. N., et al. 1986, ApJ, 301, 262
Wu, S. T., de Jager, C., Dennis, B. R., et al. 1986, ed. M. Kundu, & B. Woodgate, Energetic phenomena on the Sun, No. 2439 in NASA Conf. Publ., NASA, 5